remote sensing

MDPI

Article

Using Integrated Geodetic Data for Enhanced Monitoring of Drought Characteristics Across Four Provinces and Municipalities in Southwest China

Liguo Lu [1], Xinyu Luo [1], Nengfang Chao [2], Tangting Wu [1,*] and Zhanke Liu [3]

[1] School of Surveying and Geoinformation Engineering, East China University of Technology, Nanchang 330013, China; lglu@ecut.edu.cn (L.L.)
[2] College of Marine Science and Technology, China University of Geosciences, Wuhan 430074, China; chaonf@cug.edu.cn
[3] First Geodetic Surveying Brigade Ministry of National Resources, Xi'an 710054, China
* Correspondence: ttwu@ecut.edu.cn

Abstract: This paper presents an analysis of regional terrestrial water storage (TWS) changes and drought characteristics in Southwest China, encompassing Sichuan Province, Chongqing Municipality, Yunnan Province, and Guizhou Province. Existing geodetic datasets, such as those from the Gravity Recovery and Climate Experiment (GRACE) and its successor satellites (GRACE Follow-On), as well as Global Navigation Satellite System (GNSS) data, face significant challenges related to limited spatial resolution and insufficient station distribution. To address these issues, we propose a novel inversion method that integrates GNSS and GRACE/GFO data by establishing virtual stations for GRACE/GFO data and determining the weight values between GNSS and GRACE/GFO using the Akaike Bayesian Information Criterion (ABIC). This method allows for estimating the TWS changes from December 2010 to June 2023 and monitoring drought conditions in conjunction with hydrometeorological data (precipitation, evapotranspiration, and runoff). The results show strong correlations between TWS changes from the joint inversion and GNSS (0.98) and GRACE/GFO (0.69). The Joint Drought Severity Index (Joint-DSI) indicates five major drought events, with the most severe occurring from July 2022 to June 2023, with an average deficit of 86.133 km^3. Extreme drought primarily impacts Sichuan and Yunnan, driven by abnormal precipitation deficits. The joint inversion methodology presented in this study provides a practical approach for monitoring TWS changes and assessing drought characteristics in Southwest China. This paper leverages the complementary strengths of GNSS and GRACE/GFO data and offers new insights into regional water resource management and drought detection.

Keywords: GNSS vertical displacement; terrestrial water storage; GRACE/GFO; joint inversion; drought events

check for updates

Academic Editors: Shuanggen Jin, Mariusz Specht and Gino Dardanelli

Received: 11 December 2024
Revised: 14 January 2025
Accepted: 19 January 2025
Published: 24 January 2025

Citation: Lu, L.; Luo, X.; Chao, N.; Wu, T.; Liu, Z. Using Integrated Geodetic Data for Enhanced Monitoring of Drought Characteristics Across Four Provinces and Municipalities in Southwest China. *Remote Sens.* **2025**, *17*, 397. https://doi.org/10.3390/rs17030397

Copyright: © 2025 by the authors. Licensee MDPI, Basel, Switzerland. This article is an open access article distributed under the terms and conditions of the Creative Commons Attribution (CC BY) license (https://creativecommons.org/licenses/by/4.0/).

1. Introduction

Rising global temperatures and low precipitation frequency make drought a major natural disaster worldwide [1–3]. Due to its persistence and universality, drought seriously threatens the ecological environment and socioeconomic development. It is one of the most severe meteorological disasters that cause financial losses among many natural disasters [4]. Meteorological, hydrological, agricultural, and socioeconomic experts primarily identify drought in terms of distinct categories. Meteorological drought mainly refers to the lack of

long-term precipitation, resulting in dry climatic conditions; hydrological drought refers to the significant decrease in water bodies due to decreased precipitation or insufficient groundwater supply [5–8].

Terrestrial water storage (TWS) mainly comprises soil moisture, groundwater, lake water, and river water. Although TWS accounts for only 3.5% of the water cycle, it has an essential impact on climate and weather and is also the basis for the survival of life on Earth [9]. Therefore, monitoring TWS changes and quantifying TWS surpluses and deficits are essential for developing effective water resources management and drought response strategies.

Various geodetic techniques and hydrological models have been used to monitor changes in the TWS, including the Gravity Recovery and Climate Experiment (GRACE) and its successor GRACE Follow-On (GFO) and the Global Land Data Assimilation System (GLDAS). GRACE/GFO can monitor large-scale surface mass changes with a spatial resolution of 300–500 km and a temporal resolution at monthly intervals [10,11]. However, due to the nearly one-year data gap between GRACE and GFO, GRACE/GFO is limited in monitoring small-scale and short-term TWS changes. Although the GLDAS model can simplify complex hydrological processes through mathematical modeling, it cannot simulate all water components [12].

The emergence of the Global Navigation Satellite System (GNSS) provides another option for monitoring regional TWS changes. GNSS displacement (especially GNSS vertical displacement data) allows for continuous monitoring of the Earth's surface motion with millimeter-level accuracy to infer TWS changes [13–15]. Since its emergence, GNSS vertical displacement inversion for TWS changes has been widely applied in hydrological and geodetic research [16]. Currently, researchers employ two main methods to establish the relationship between TWS changes and surface deformation [17]. One is Green's function method based on the spatial domain [13], and the other is the Slepian basis function method based on the frequency domain [18]. Many scholars have studied the TWS changes around the world based on the above two methods [8,19–23], and the results show that the use of GNSS vertical displacement alone can continuously obtain the Earth's load changes in days or months within 50–100 km.

The density of GNSS stations restricts the quality of GNSS inversion TWS change results [24]. When GNSS stations are unevenly distributed, the inversion results will be unstable. Therefore, to weaken and solve this impact, researchers combined GNSS, GRACE/GFO, and other hydrological models to obtain more accurate regional TWS changes for various studies. Fok et al. [25] and Liu et al. [26] proposed a new method of setting up virtual stations, which calculates the TWS obtained from GRACE as the vertical displacements of these virtual stations and uses them as supplementary virtual stations for inversion together with the GNSS stations to enhance the density of the GNSS stations. Li et al. [27] and Zhu et al. [28] also adopted the above method to analyze the TWS changes in the Yangtze River Basin and Yunnan Province. Adusumilli et al. [29] used GRACE-TWS as a constraint in the regularization process of GNSS inversion to obtain higher spatiotemporal resolution results. Carlson et al. [30] employed JPL Mascon to construct limitations to make them more consistent with the actual spatial resolution of GRACE. Yang et al. [31] improved the two types of joint methods (setting the virtual station method and using GRACE/GFO as the spatial constraint method), indicating that the joint methods can integrate the spatial sensitivity advantages of GNSS and GRACE/GFO.

Southwest China (including Sichuan Province, Chongqing Municipality, Yunnan Province, and Guizhou Province) has a complex topography and geomorphology structure. The precipitation here is subject to seasonal changes, resulting in uneven spatiotemporal distribution and significant differences between dry and wet seasons. With the impact of

global warming, this region has experienced a substantial decrease in precipitation and an increase in temperature, leading to frequent droughts [32]. Researchers primarily focus on meteorological drought in Southwest China [33], while few studies address the interplay between comprehensive meteorological drought and hydrological drought [28,34,35]. In order to more comprehensively reveal the relationship between meteorological factors (such as precipitation anomalies) and hydrological variables (such as TWS) and analyze their different roles in drought detection in Southwest China, we combine hydrological drought factors and meteorological drought factors for joint analysis. This study primarily employs the standardized precipitation evapotranspiration (SPEI) index as the basis for the meteorological drought index, considering multi-scale factors such as temperature change, solar radiation, wind speed, and humidity [36]. Since GNSS vertical displacement serves as a tool for monitoring water storage surpluses and deficits caused by drought and floods, it can be combined with the drought index to analyze drought events [37]. Subsequently, Jiang et al. [34] proposed the GNSS drought index (GNSS-DSI) to analyze the drought situation in Yunnan, which was calculated based on the TWS change obtained from GNSS inversion alone. Li et al. [35] adopted the results of the GNSS and GRACE/GFO joint inversion to analyze the extreme flood disasters in Sichuan from 2020 to 2022. Peng et al. [38] obtained the GNSS-DSI of Poyang Lake Basin at the daily scale based on the GNSS inversion of daily TWS changes and then analyzed the drought situation in the basin. Zhu et al. [39] integrated GNSS observation data with precipitation metrics to compute precipitation efficiency (PE) and drought index, facilitating a comprehensive analysis of the drought conditions in Guangdong Province. This paper uses the Joint-DSI calculated by the joint inversion of TWS changes as the hydrological drought index.

In this study, we take Southwest China (SCP, YNP, GZP, and CQM) as the study area and set up GRACE/GFO virtual stations in the whole research area. We use Akaike's Bayesian information criterion (ABIC) to determine the relative weight factor between the GNSS and GRACE/GFO, as well as the smoothing factor of prior constraints, to invert the TWS of the research area. Comparison of the results with the TWS obtained using GNSS inversion alone (including Green's function method and the Slepian basis function method) and GRACE/GFO Mascon solutions reveal that the TWS derived from four methods maintain good correlation on both time and spatial scales. In addition, we also compare and validate the dTWS/dt obtained from the joint inversion with the TWS changes estimated by the water balance equation (P-ET-R). We comprehensively analyzed the drought events during the period December 2010 to June 2023 from both meteorological and hydrological perspectives. Finally, we conducted a quantitative study on drought events across four provinces and municipalities in Southwest China regarding drought frequency, drought severity, and the classification of droughts and floods.

2. Materials and Methods

2.1. Data

2.1.1. Study Area

The study area is located in Southwest China (Figure 1), encompassing Sichuan Province (SCP), Yunnan Province (YNP), Chongqing Municipality (CQM), and Guizhou Province (GZP), covering a total area of about 1.13×106 km^2. The topography of Southwest China is intricate, predominantly mountainous or hilly, with a terrain primarily defined by its high northwest and low southeast elevation. The prevalent climate types are the subtropical humid monsoon climate, the subtropical plateau monsoon humid climate, and the distinctive plateau climate akin to the Qinghai–Tibet Plateau [32]. Moreover, precipitation exhibits uneven spatial and temporal distributions, with it being more abundant in summer and autumn, scarce in winter and spring, and predominantly concentrated

in the southwest region. Due to global warming, precipitation in Southwest China has significantly declined, leading to frequent drought occurrences that have severely impacted local agricultural production. Consequently, conducting drought detection and research in Southwest China is imperative.

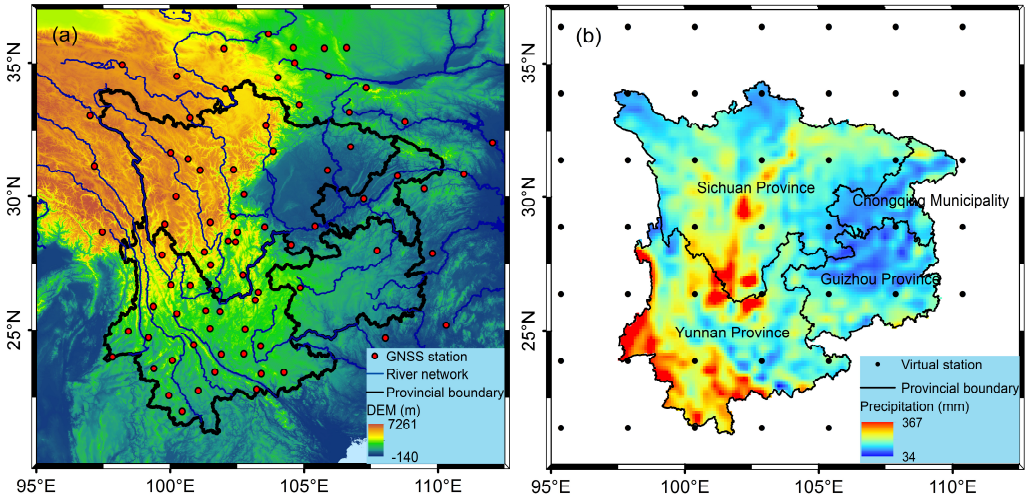


Figure 1. (**a**) Geographical overview of Southwest China and distribution of GNSS stations. The red circle represents the GNSS station of the China Crustal Movement Observation Network (CMONOC), the blue line represents the river network, the thick black line represents the provincial boundary, and the background is the digital elevation model (DEM). (**b**) Annual precipitation amplitude and GRACE/GFO virtual station distribution map in Southwest China. The black circle represents the GRACE/GFO virtual station, and the background is the annual precipitation amplitude.

2.1.2. GNSS Vertical Displacement Time Series

From the GNSS vertical displacement time series provided by the China Crustal Movement Observation Network (CMONOC) (http://www.eqdsc.com, accessed on 1 May 2024), we selected the vertical displacement time series of 79 stations in the southwest region for processing from December 2010 to June 2023. Figure 1 illustrates the distribution of stations, with an average distance of nearly 120 km between 79 stations; the distribution of stations is uneven, mainly in the west (SCP and YNP) and, sparsely, in the east (GZP and CQM). The data provided by the CMONOC performed baseline processing through GAMIT/GLOBK10.70 [40] and overall adjustment using QOCA software [41], ultimately obtaining the time series within the ITRF2008 framework.

Post-processing is needed to obtain a continuous and stable GNSS vertical displacement time series based on hydrological signals. Firstly, we employ the least-squares fitting method to eliminate data jumps, and then we apply the quartile range gross error detection method to remove gross errors. The Kriging Kalman filter interpolation software is used to find missing data [42]. In addition, to obtain GNSS observations dominated by hydrological signals, we use the non-tidal atmospheric load (NTAL) and non-tidal ocean load (NTOL) models under the geometric center reference framework (CF) provided by the German Research Centre for Geosciences (GFZ) to deduct the effects of atmospheric load and ocean load (http://esmdata.gfz-potsdam.de:8080/repository, accessed on 30 May 2024). The annual amplitude of NTAL is 1.5~5.5 mm, and the yearly amplitude of NTOL is 0.1~0.6 mm (Figure S1). Finally, the annual amplitude of the GNSS station is 1~10 mm. Figure 2 compares the vertical displacement time series of four stations in Southwest China before and after post-processing. After the above post-processing, we get a complete and clean time series. Therefore, post-processing of the original GNSS time series is significant for the subsequent use of GNSS data to obtain TWS changes.

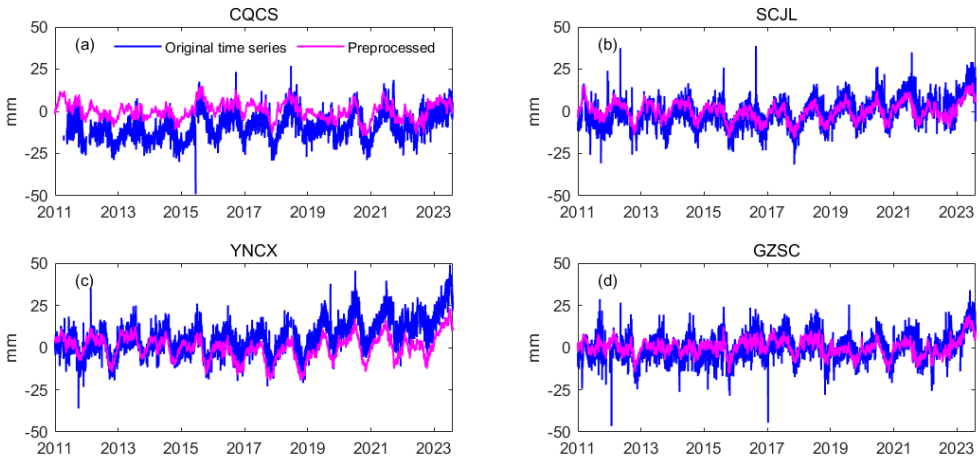


Figure 2. Vertical displacement time series of four stations before and after preprocessing. The blue solid line represents the original time series, and the red solid line represents the time series obtained after preprocessing. (**a**) CQCS station; (**b**) SCJL station; (**c**) YNCX station; (**d**) GZSC station.

2.1.3. GRACE/GFO Mascon Solutions

This paper used the GRACE/GFO Mascon solutions released by the Center for Space Research (CSR) at the University of Texas at Austin to estimate the TWS changes in Southeast China [43] (https://www2.csr.utexas.edu/grace/RL06_mascons.html, accessed on 1 June 2024). The CSR Mascon solutions have applied all appropriate corrections, including C20 and C30 replacements, first-order geocentric corrections, and glacial isostatic adjustment [44]. Since the GRACE data were cut off in June 2017 and GFO was launched in May 2018, nearly one year of missing data occurred. This paper did not fill in the corresponding missing data; the remaining missing data were completed using the cubic spline interpolation method.

2.1.4. Hydrometeorological Data

Multi-source hydrometeorological data can help us to verify the inversion results using geodetic data. In this study, monthly precipitation (P), evapotranspiration (ET), and runoff (R) data with a spatial resolution of 0.1° × 0.1° are utilized, which are provided by ERA5-Land (https://cds.climate.copernicus.eu/, accessed on 30 June 2024). ERA5-Land is produced by redrafting the land portion of ERA5 climate reanalysis data from the European Centre for Medium-Range Weather Forecasts (ECMWF) [45]. GLDAS NOAH provides monthly P, ET, and R data with a spatial resolution of 0.25° × 0.25° [46] (https://disc.gsfc.nasa.gov/, accessed on 30 June 2024). The Global Precipitation Climate Project (GPCP) provides monthly P data with a spatial resolution of 2.5° × 2.5° derived from the combinations of satellite estimation and land rain gauge measurements [47] (https://www.ncei.noaa.gov/, accessed on 30 June 2024). The Global Land Evaporation Amsterdam Model (GLEAM) provides monthly ET data with a spatial resolution of 0.1° × 0.1°, which can maximize the extraction of evaporation information from climate and environmental variables observed by different satellites [48] (https://www.gleam.eu/, accessed on 30 June 2024). The monthly P data from the three datasets are consistent between December 2010 and June 2023, with GLEAM providing significantly smaller ET data than ERA5 and NOAH and ERA5 providing considerably smaller R data than NOAH. As shown in Figure 3, the P, ET, and R data in Southwest China exhibit obvious seasonal variations, all peaking in the summer of each year. However, the magnitude of the P time series is much larger than that of ET and R, indicating that the P data significantly impacts the TWS change here more than the other two data.

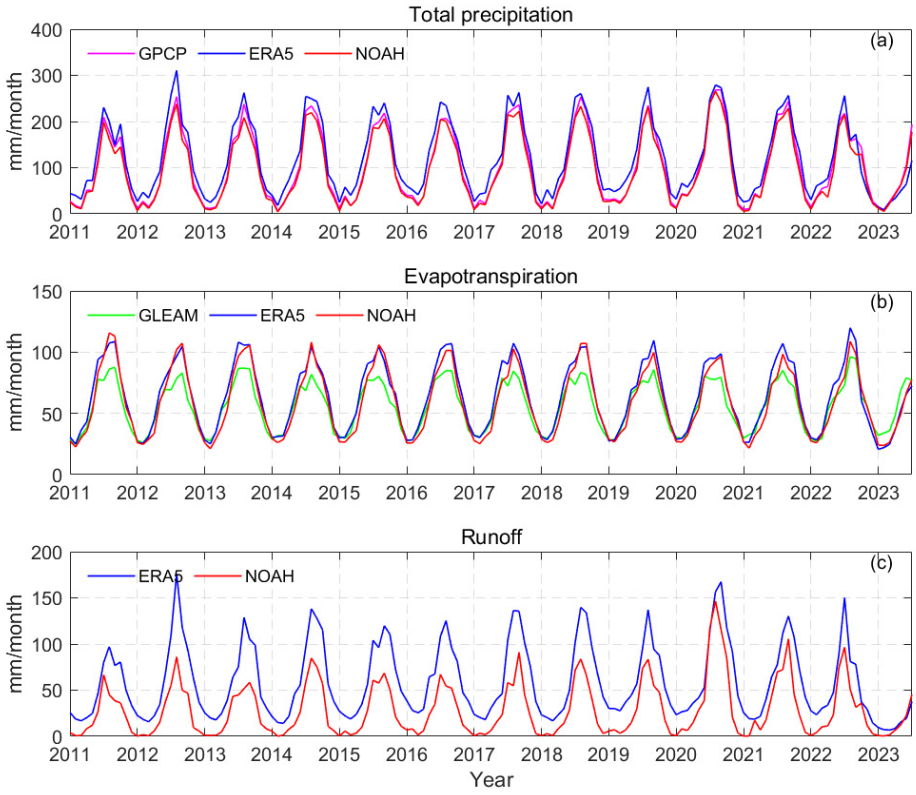


Figure 3. Multi-source precipitation (**a**), evapotranspiration (**b**), and runoff data (**c**).

In order to verify the correctness of the TWS change results, this paper quantifies TWS changes based on the water balance equation [31,49].

$$dTWS/dt = P - ET - R \tag{1}$$

The TWS changes obtained from GNSS, GRACE/GFO, and joint inversion are calculated as the first-order differential to time, as follows:

$$dTWS/dt = TWS(t+1) - TWS(t) \tag{2}$$

The TWS change calculated by P, ET, and R represents the change in the middle of each month. In contrast, the TWS first-order differential calculated using Equation (2) represents the TWS change at the beginning or end of the month. To ensure the consistency of time, this paper adopts the time series filtering method proposed by Landerer et al. [50] to filter P-ET-R:

$$\hat{F}(t) = \frac{1}{4}F(t-1) + \frac{1}{2}F(t) + \frac{1}{4}F(t+1) \tag{3}$$

where F denotes P, ET, and R, and $\hat{F}$ denotes the filtered data.

The SPEI selected in this paper is provided by the Climate Research Center (CRU) at the University of East Anglia (https://digital.csic.es/, accessed on 30 June 2024).

2.2. Methods

2.2.1. Green's Function

According to the mass loading theory, Farrell proposed that TWS changes can cause the elastic deformation of the surface, and their relationship can be expressed by a linear equation as follows [13]:

$$d_1 = G_1 x_1 + e_1 \tag{4}$$

where x_1 represents the mass loading vector expressed as the equivalent water height (EWH); d_1 represents the GNSS displacement vector; e_1 represents the error term; G_1 represents the calculated Green's function. Argus et al. proposed the least-squares model for GNSS vertical displacement inversion of TWS as follows [19]:

$$\left\|{\sigma_1}^{-1}(G_1 x_1 - d_1)\right\|^2 + \beta^2 \|L(x_1)\|^2 \rightarrow \min \tag{5}$$

$$E = {\sigma_1}^2 \tag{6}$$

where σ_1 denotes the standard deviation; since the GNSS observations are less than the EWH grids, it is necessary to add the Laplace spatial smoothing constraint to the inversion model, so L represents the Laplace operator; β is the regularization factor determined by the Generalized Cross-Validation (GCV) method, with a value of 0.29 (Figure S2). Using the least-squares algorithm, we divide the study area into $0.5^\circ \times 0.5^\circ$ grids, then the EWH value of each grid can be calculated as follows:

$$\hat{x}_1 = \left({G^T}_1 E^{-1} G_1 + \beta L^T L\right)^{-1} {G^T}_1 E^{-1} d_1 \tag{7}$$

2.2.2. Slepian Basis Function

Han and Razeghi proposed to estimate the spectral information of the GNSS displacement through a regional spherical basis function [18] and apply the loading Love number to obtain the EWH of the region, which can be expressed as follows:

$$\sigma_L(\theta, \lambda, t) = a \sum_{\beta=1}^{J} \gamma_\beta s_\beta^{EWH}(t) g_\beta(\theta, \lambda) \tag{8}$$

where a is the Earth's radius; J is the truncation order; γ_β denotes the eigenvalue; s_β^{EWH} is the Slepian basis function coefficients; g_β is the Slepian basis function. Figure S3 displays the concentration ratio of each Slepian basis function. Figure S4 represents the energy spatial distribution of Slepian basis functions, with the black solid line indicating the boundary of the study region after an extension of 2°. The first 28 basis functions with concentration ratios greater than 0.1 are well concentrated in Southwest China. According to research by Li et al. [22], the average distance between GNSS stations serves as a suitable radius for Gaussian filtering. Given that the average distance between GNSS stations in this study is approximately 120 km, we set the radius of Gaussian filtering to 150 km. The minimum and maximum distances between adjacent stations are about 50 km and 323 km, while the value 65 is close to the ratio of 20,000/323 km (wherein 20,000 km represents half of the Earth's circumference), so the maximum order in this paper is set to 65.

2.2.3. Joint Inversion

This paper employs a joint inversion model founded on incorporating virtual stations, as advocated by Fok et al. [25] and Liu et al. [26]. By integrating this with the modified mathematical model proposed by Yang et al. [31], we strategically establish virtual stations across the entire study region and introduce a weighting factor to ascertain the optimal balance between GNSS and GRACE/GFO datasets, thereby mitigating the risk of overfitting. The TWS derived from GRACE is inverted to the vertical displacement of the GNSS virtual station and then performs inversion together with the GNSS station to augment its density. The following expression outlines the displacement inferred from the forward model of GRACE/GFO:

$$d_2 = G_2 x_2 + e_2 \tag{9}$$

where d_2 is the displacement vector calculated by GRACE/GFO; G_2 is the Green's function of the GRACE/GFO virtual station; x_2 is the corresponding GRACE/GFO solution in the study area; e_2 denotes the error term. In order to determine the location and number of GRACE/GFO virtual stations, this paper uses the checkerboard test to investigate the spatial resolution of TWS inversion by virtual stations [24]. The results show that we can recover the grid signal with a spatial resolution of 3.5° × 3.5° by deploying GRACE/GFO virtual stations at an interval of 2.5° in Southwest China (Figure S5), which matches the original spatial resolution of GRACE/GFO (~350 km). Therefore, this paper evenly distributes 56 GRACE/GFO virtual stations in the study area at 2.5° intervals. The virtual station distribution method is also applicable to the virtual station settings in Sichuan and Yunnan [31].

The displacement and Green's function of GRACE/GFO are obtained from the forward model, composing new observation data as follows:

$$d = \begin{pmatrix} d_1 & d_2 \end{pmatrix}^T \tag{10}$$

$$G = \begin{pmatrix} G_1 & G_2 \end{pmatrix}^T \tag{11}$$

GNSS and GRACE/GFO are two independent data types; we introduce the weighting factor α to obtain the variance matrix:

$$E(\hat{\alpha}^2) = \begin{pmatrix} \alpha^2\sigma_1^2 & 0 \\ 0 & {\sigma_2}^2 \end{pmatrix} \tag{12}$$

By bringing the above observations into the least-squares model of Equation (5), we can obtain the EWH value of each grid calculated by the joint inversion:

$$\hat{x} = \left(G^T E\left(\hat{\alpha}^2\right)^{-1} G + \hat{\beta} L^T L\right)^{-1} G^T E\left(\hat{\alpha}^2\right)^{-1} d \tag{13}$$

This paper employs the ABIC method to ascertain the weight factors within the joint inversion model. The ABIC is an objective method based on the principle of entropy maximization, integrating the Akaike information criterion with the Bayesian theorem [51], and is commonly used to determine the weight factor in geodetic inversion [25,31,35,52]. By solving the minimum value of the ABIC function, we can effectively estimate the optimal weights between GNSS and GRACE/GFO data.

$$\begin{aligned} ABIC(\alpha^2, \beta^2) = n \log f(\hat{x}) + \log\left\| G^T E(\hat{\alpha}^2)^{-1} G + \beta^T L^T L \right\| - \log\left\| \beta^T L^T L \right\| + \\ \log\left\| E(\hat{\alpha}^2) \right\| + C \end{aligned} \tag{14}$$

$$f(\hat{x}) = (Gx - d)^T E(\hat{\alpha}^2)^{-1} (Gx - d) + x^T \beta^2 L^T L x \tag{15}$$

where n is the number of observations; $\hat{x}$ is calculated by Equation (13); C is a constant. By seeking the minimum value of the ABIC function, the optimal weighting factors α and β can be determined. Figure 4 illustrates the distribution of ABIC values in May 2023. The minimum value of ABIC occurs at $\log(\alpha^2) = 0.69$ and $\log(\beta^2) = -2$, and then the optimal weighting factor is obtained.

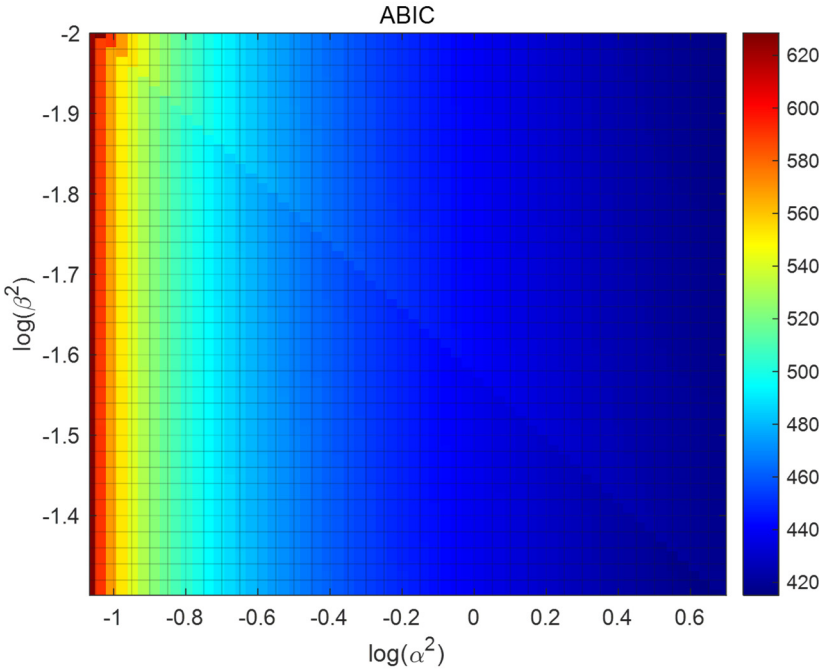


Figure 4. ABIC value distribution.

2.2.4. Drought Index

The GNSS-DSI is developed by Jiang et al. [34] based on the GRACE-DSI [53]. Table S1 lists the classification of drought severity.

The calculation of the GNSS-DSI is as follows:

$$GNSS - DSI_{i,j} = \frac{EWH_{i,j} - \overline{EWH_j}}{\sigma_j} \tag{16}$$

where $EWH_{i,j}$ represents the water storage in the j-month of the i-year; $\overline{EWH_j}$ represents the average of the j-month of each year; σ_j represents the standard deviation of the j-month of each year.

In addition, Jiang et al. [34] proposed a method for quantitatively measuring the occurrence, end, and duration of hydrological drought and drought severity by using the TWS changes. First, we need to calculate the monthly average TWS changes:

$$\overline{TWS_j} = mean \sum_{i=2010}^{2023} TWS_{i,j} \tag{17}$$

Then, we define the monthly water deficit as the difference between $TWS_{i,j}$ and $\overline{TWS_j}$:

$$DTWS_{i,j} = TWS_{i,j} - \overline{TWS_j} \tag{18}$$

Finally, we calculate severity $S(t)$ as the product of the average monthly water deficit $\overline{M}(t)$ and the duration $D(t)$:

$$S(t) = \overline{M}(t) \times D(t) \tag{19}$$

The methodological framework adopted in this study is shown in Figure 5.

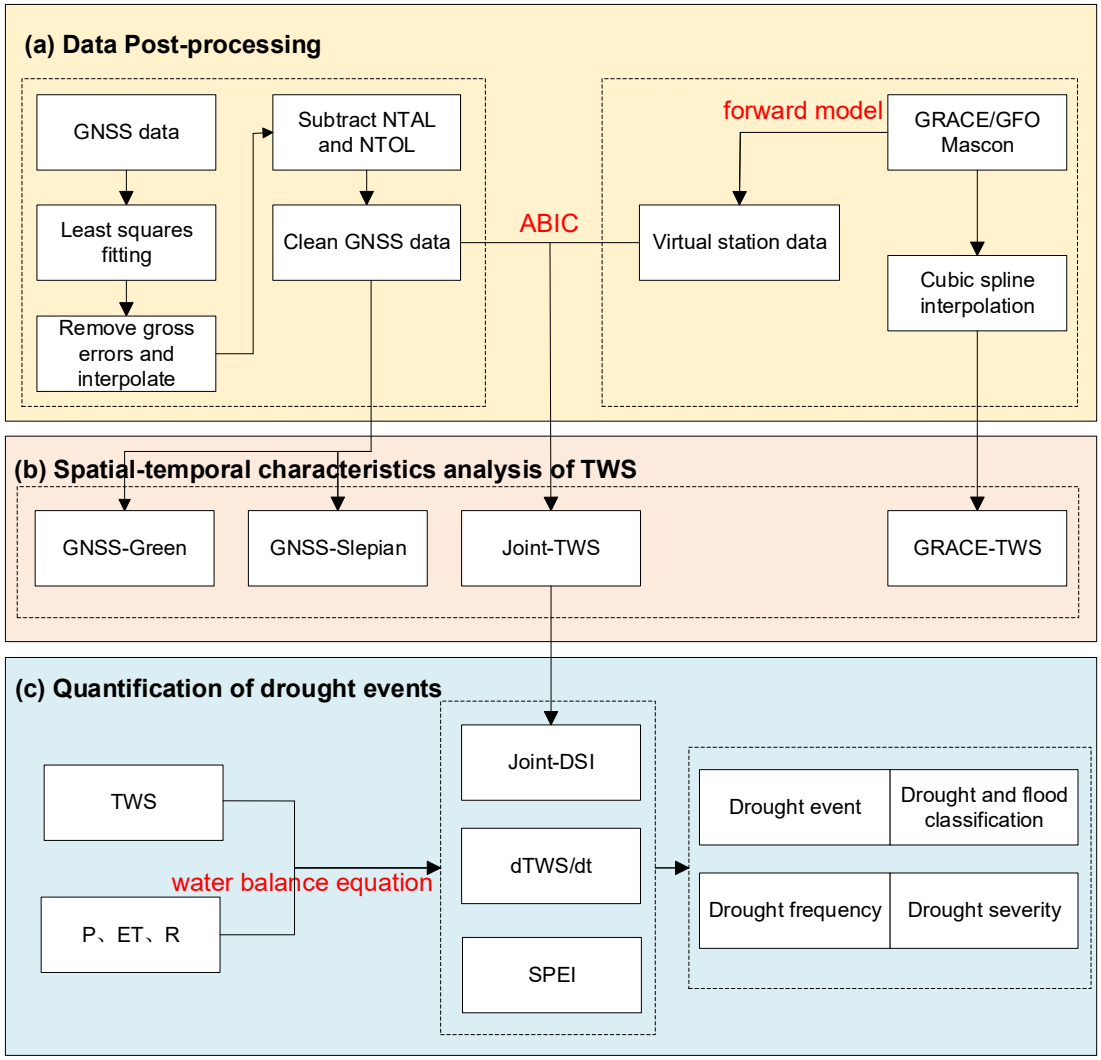


Figure 5. Methodological framework. (**a**) Data Post-processing; (**b**) Spatial-temporal characteristics analysis of TWS; (**c**) Quantification of drought events.

3. Result

3.1. Spatial Distribution Characteristics of TWS

Figure 6 illustrates the annual amplitudes of TWS derived from GNSS-Green, GNSS-Slepian, GRACE, and Joint methods in Southwestern China from December 2010 to June 2023. All methods consistently pinpoint the peak annual amplitudes to the southwest of our study area (i.e., southwest of YNP), with a maximum amplitude of about 284 mm for GNSS-Green, 325 mm for GNSS-Slepian, and 208 mm for GRACE. GNSS-Green and GNSS-Slepian exhibit strong spatial distribution coherence, given that both methods rely solely on GNSS data for inversion (Figure 6a,b). Their spatial distribution patterns reveal that the TWS annual amplitude generally tapers off from west to east, but variations in magnitude occur, with GNSS-Slepian results 25% higher than those of GNSS-Green [22,54]. According to Argus et al. [19], the GNSS vertical displacement results from the combined effect of all hydrological loads within a radius of 50 km around the GNSS station; however, the mathematical model of the Slepian basis function theoretically concentrates all hydrological influences on the GNSS station, resulting in biased inversion results.

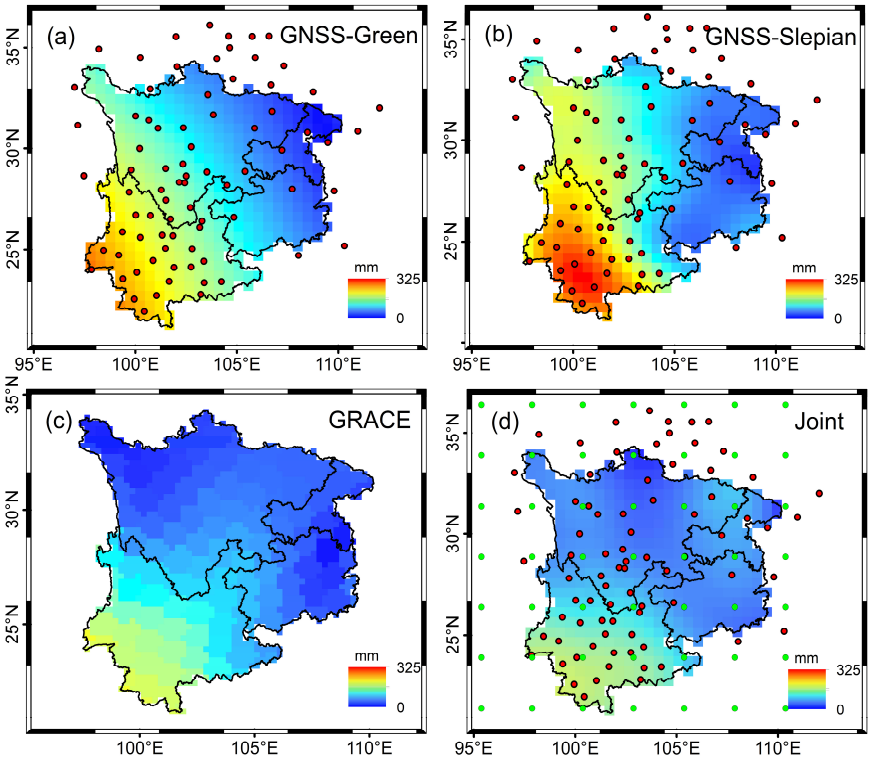


Figure 6. Spatial distribution of TWS annual amplitude obtained by different inversion methods in Southwest China from December 2010 to June 2023. The red dots indicate the GNSS stations, and the green dots indicate the GRACE/GFO virtual stations. (**a**) Spatial distribution of TWS annual amplitudes derived from GNSS-Green; (**b**) Spatial distribution of TWS annual amplitudes derived from GNSS-Slepian; (**c**) Spatial distribution of TWS annual amplitudes derived from GRACE; (**d**) Spatial distribution of TWS annual amplitudes derived from Joint method.

The spatial distribution of GNSS inversion results diverges from that of GRACE-TWS. Although the peak of the TWS annual amplitude is located in the southwest of YNP, the nuanced spatial distribution patterns differ markedly. GRACE-TWS demonstrates an escalating amplitude trend from north to south, while GNSS inversion results exhibit an amplitude increase from east to west, aligning with the trend in the GNSS vertical displacement's annual amplitude variation (Figure S1c). This may be due to the sparse distribution of GNSS stations in the northeast of the study area. In contrast, GNSS stations are more densely clustered in the central part of SCP and the northern region of YNP, enabling the GNSS to capture TWS signals in these localized areas more accurately. In these regions, GRACE-TWS struggles to discern TWS changes. Consequently, GNSS inversion results are better equipped to accurately capture TWS changes in areas with dense GNSS station coverage, particularly in higher-altitude plateau regions. Conversely, GRACE-TWS, constrained by its relatively low resolution [21], proves more reliable in areas with a sparse GNSS station distribution. The GZS region only contains two GNSS stations with an average station distance of 300 km, which aligns with GRACE/GFO's large-scale spatial resolution. GRACE-TWS here is 60.4 mm, but for Green-TWS, the value is 93 mm, for Slepian-TWS, 71.8 mm, and for Joint-TWS, 70.4 mm, respectively. Therefore, the deviation between Joint-TWS and GRACE-TWS is the smallest, while between Green-TWS and GRACE-TWS, it is the largest. This result indicates that Green-TWS has the most significant effect on station distribution, and the joint inversion method can effectively reduce the error caused by the sparse distribution of GNSS stations. In sparse GNSS station regions, Joint-TWS mitigates the effects of limited GNSS station availability on inversion results,

thereby enhancing their reliability. At the same time, it retains the advantages the GNSS provides in areas with a dense station distribution.

Figure 7 depicts the annual phases derived from GNSS-Green, GNSS-Slepian, GRACE, and Joint methods spanning from December 2010 to June 2023. The annual phases obtained by these four methods manifest commendable spatial coherence, except for GNSS-Green, which shows significant divergence in the east of the study area, such as CQM.

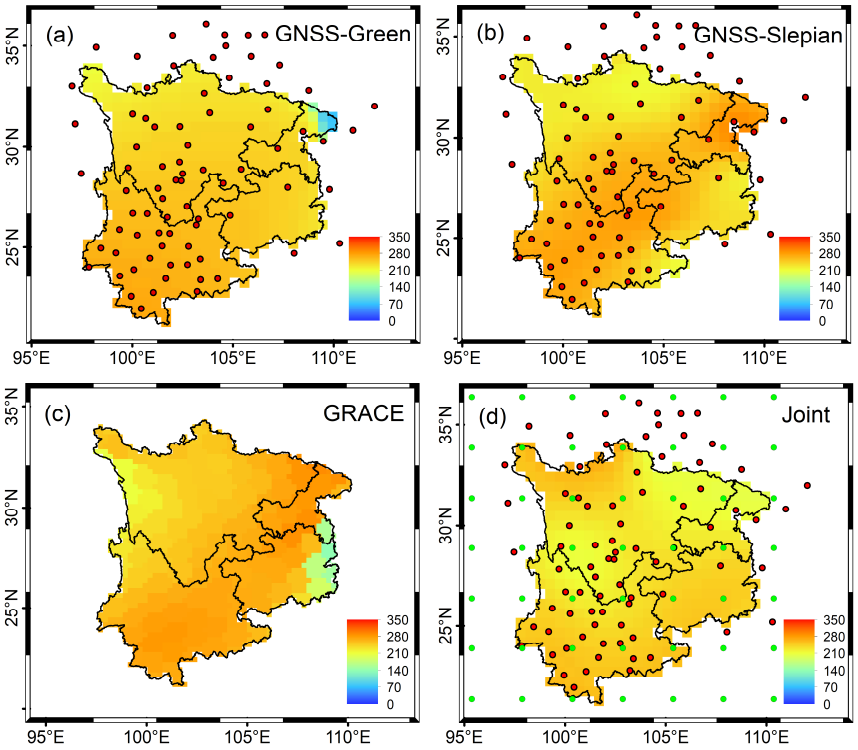


Figure 7. Spatial distribution of TWS annual phase obtained by different inversion methods in Southwest China from December 2010 to June 2023. The red dots indicate the GNSS stations, and the green dots indicate the GRACE/GFO virtual stations. (**a**) Spatial distribution of TWS annual phase derived from GNSS-Green; (**b**) Spatial distribution of TWS annual phase derived from GNSS-Slepian; (**c**) Spatial distribution of TWS annual phase derived from GRACE; (**d**) Spatial distribution of TWS annual phase derived from Joint method.

3.2. Temporal Distribution Characteristics of TWS

To further delve into the validity of the joint inversion results and the distinctions among various inversion methods, we investigate the dTWS/dt time series derived from GNSS-Green, GNSS-Slepian, GRACE, Joint methods, precipitation data, and water balance equations. Figure 8a illustrates the average time series of TWS inferred by GNSS-Green, GNSS-Slepian, GRACE, Joint methods, and precipitation within Southwest China, which manifests obvious seasonal patterns. The results reveal that the two time series of TWS changes obtained by pure GNSS inversions exhibit remarkable consistency with a correlation coefficient of 0.98. Nevertheless, GNSS-Slepian results are quantitatively more prominent than those derived from GNSS-Green. Additionally, the time series of TWS changes extracted from pure GNSS inversion is approximately threefold that of GRACE/GFO, with correlation coefficients of 0.82 and 0.79, respectively. The value of the joint inversion results resides between the two, and the trend aligns more closely with that of GRACE/GFO, exhibiting a correlation coefficient of 0.83. Compared to the results derived from pure GNSS inversion, the trajectory of the joint inversion results approximates more faithfully that of GRACE/GFO. In contrast to the trend of precipitation data, the geodetic datasets demonstrate commendable consistency. Nevertheless, the intricate transport mechanisms

of terrestrial water potentially cause a delay of 1 to 2 months in the apex value of the geodetic dataset relative to the precipitation data [8,21,31,55]. Since 2023, TWS fluctuations across various geodetic datasets have diminished substantially. Subsequent analysis reveals that this occurrence is predominantly a consequence of the sharp decline in precipitation during this period, which plummeted to a mere 45% of the levels recorded in corresponding periods of prior years. The impact of precipitation on the results of GNSS inversion is markedly more pronounced than that exerted by GRACE/GFO data. Figure 8b shows the time series of dTWS/dt derived from GNSS-Green, GNSS-Slepian, GRACE, and Joint methods. Table 1 presents the correlation coefficients between dTWS/dt derived from various datasets, revealing a robust correlation among the geodetic datasets. Nevertheless, we could ascribe the more pronounced variation in dTWS/dt yielded by using GNSS exclusively for TWS inversions to the heightened sensitivity of the GNSS in discerning anomalous TWS changes.

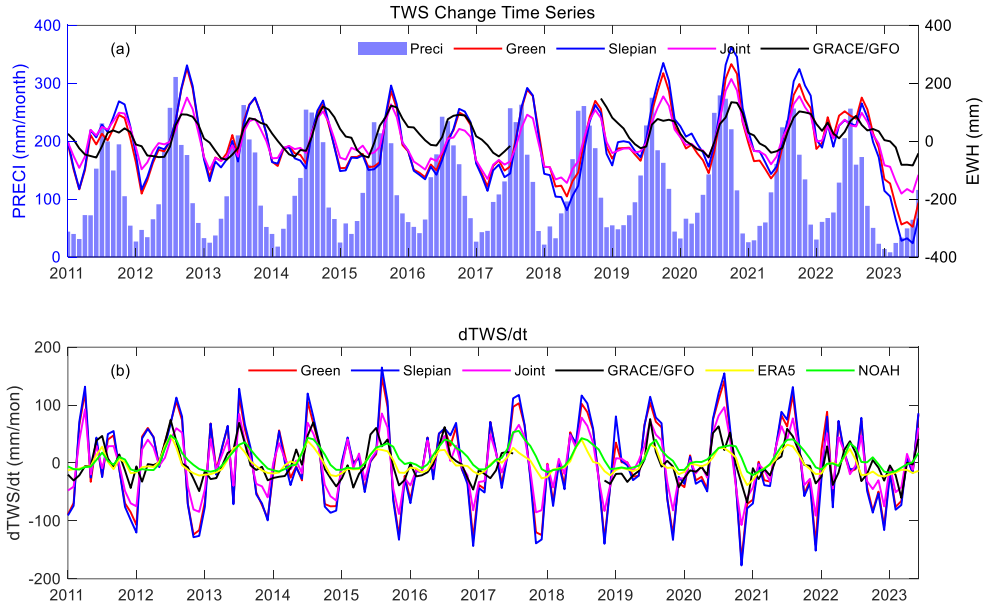


Figure 8. (**a**) Time series of TWS changes and precipitation obtained by GNSS-Green, GNSS-Slepian, GRACE, and Joint methods; (**b**) time series of dTWS/dt derived from GNSS-Green, GNSS-Slepian, GRACE, Joint methods, and ERA5 datasets and NOAH data.

Table 1. Correlation coefficients between dTWS/dt obtained from different datasets.

	GNSS-Green	GNSS-Slepian	Joint-TWS	GRACE-TWS	ERA5	NOAH
GNSS-Green	-	-	-	-	-	-
GNSS-Slepian	0.99	-	-	-	-	-
Joint-TWS	0.98	0.98	-	-		-
GRACE-TWS	0.66	0.66	0.69	-	-	-
ERA5	0.61	0.62	0.62	0.79	-	-
NOAH	0.49	0.51	0.49	0.76	0.85	-

The trend of dTWS/dt derived from geodetic data is similar to that of P-ET-R, but the amplitude is noticeably more significant than that of P-ET-R, suggesting that the P-ET-R calculated via the water balance equation may somewhat underestimate the changes in TWS within the region. This discrepancy may arise because P-ET-R does not account for the influence caused by deep groundwater composition or human activities [22]. These activities can significantly alter the local water balance, especially in areas where water withdrawals exceed recharge. In addition, discrepancies in model parameterization, particularly in soil

water retention, infiltration rates, and groundwater flow, may lead to differences between TWS derived from the water balance equation and geodetic-inferred TWS. Compared to the P-ET-R determined using NOAH data (0.49~0.76), the TWS differentials obtained from geodetic data exhibit a stronger correlation with those calculated from ERA5 data (0.69~0.79). This elevated correlation could be attributed to the superior spatial resolution of ERA5 data, providing more detailed and precise meteorological information, whereas the NOAH model is based on the simulation of land surface processes, constrained by the model's underlying assumptions and parameter configurations. Compared with the results from utilizing the GNSS alone to infer TWS changes, the correlation coefficient between Joint methods and other alternatives demonstrates a higher degree of association. In the subsequent investigation of drought events in Southwest China, this paper adopts the Joint-DSI results as the hydrological and meteorological drought index to facilitate comparative and analytical endeavors.

3.3. GNSS-Based Drought Index

We delineate an event as a hydrological drought when the water deficit persists for three months or more. Our joint inversion analysis results derive the data in Table 2. Our findings reveal five distinct drought events in the southwestern region from December 2010 to June 2023. The most prolonged event transpired from January 2016 to December 2018, lasting 36 months. The most acute single drought event occurred in September 2022, exhibiting an average deficit of 86.133 km^2.

Table 2. Drought events and severity inferred by Joint-TWS in Southwest China from December 2010 to June 2023.

Occurrence Time	Duration (Month)	Peak Deficit (km^3)	Average Deficit (km^3)	Total Severity (km^3)	Correlation Coefficient
August 2013–December 2013	5	−50.817 (October 2013)	−32.899	−164.499	0.67
June 2014–January 2015	8	−22.758 (October 2014)	−13.223	−105.782	0.78
May 2015–August 2018	4	−56.075 (July 2015)	−23.912	−95.649	0.81
January 2016–December 2018	36	−111.192 (April 2018)	−39.177	−1410.370	0.61
September 2022–June 2023	10	−150.694 (May 2023)	−86.133	−861.332	/

Given the pronounced topographic differences in Sichuan Province (SCP), Yunnan Province (YNP), Chongqing Municipality (CQM), and Guizhou Province (GZP), coupled with the substantial variations in the spatial distribution of precipitation, we have elected to undertake a meticulous analysis to evaluate the drought attributes of these areas more thoroughly. This analysis aims to provide a more precise depiction of the specific drought conditions across four provinces and municipalities in Southwest China, thus allowing us to understand the impact of topography and precipitation distribution on drought conditions. Figure 9 presents the time series of the Joint-DSI, SPEI, and precipitation deficits for SCP, YNP, CQM, and GZS. While there are variations between the meteorological drought index (i.e., SPEI) and the hydrological drought index (i.e., Joint-DSI) throughout the study period, the trend remains congruent during instances of severe drought (when the drought index falls below −1.3). The changes in the Joint-DSI marginally lag behind the SPEI, as the meteorological drought index is typically more responsive than its hydrological counterpart. The meteorological index offers a direct reflection of alterations in precipitation, whereas the hydrological index necessitates intricate computations via processes such as the hydrological cycle to ascertain drought occurrences. As a result, the SPEI demonstrates a stronger correlation with fluctuations in precipitation than the Joint-DSI. Compared to

the results in Table 2, Figure 9 affords more details on the temporal patterns of drought occurrence in Southwest China. Table 2 scrutinizes the southwest region and estimates five drought incidents based on fluctuations in TWS. Nonetheless, juxtaposing this with Figure 9 unveils significant disparities across the different regions. Specifically, Yunnan remained unscathed by severe drought conditions throughout the prolonged drought period from January 2016 to December 2018. Consequently, a more nuanced analysis of the drought situation in Southwest China is imperative in conjunction with insights from Figure 9.

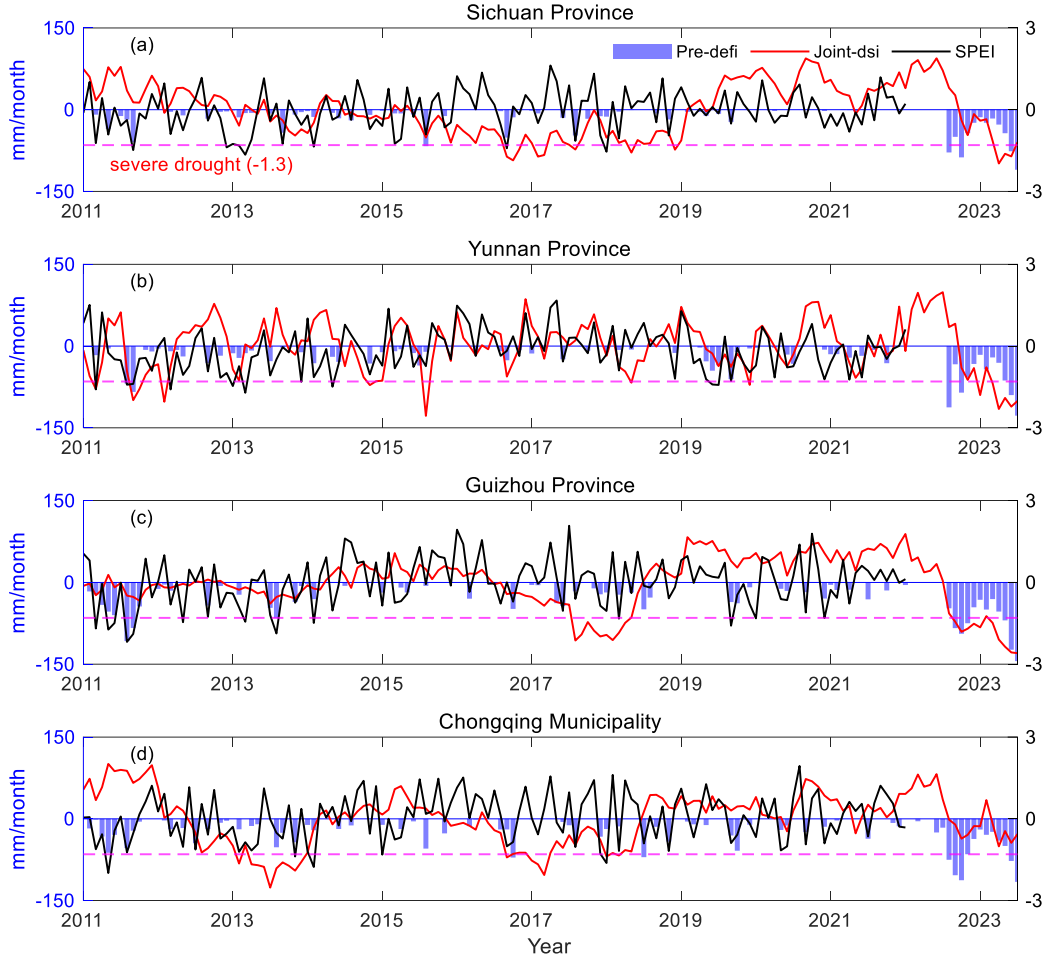


Figure 9. Temporal variations in the Joint-DSI, SPEI, and precipitation deficit on a monthly scale across four provinces and municipalities in Southwest China. (**a**) Drought index for Sichuan Province; (**b**) Drought index for Yunnan Province; (**c**) Drought index of Guizhou Province; (**d**) Drought index of Chongqing Municipality.

This investigation concentrates on the spatial evolution of drought events within Southwest China from June 2022 to June 2023. Figure S6 elucidates the comprehensive spatial developmental trajectory of the Joint-DSI during this drought episode. We can discern that, throughout this interval, a substantial portion of the southwest region remains enshrouded in a state of drought. Nonetheless, the overall intensity of drought characterized by CQM remains relatively modest, an observation that resonates with Figure 9d. The locales exhibiting the most pronounced drought conditions are situated southwest of YNP, west of SCP, and at the confluence of GZP and YNP. This spatial configuration mirrors the spatial distribution of TWS annual amplitude, as shown in Figure 6. Since February 2022, the drought has escalated in severity, possibly attributable to the increasing precipitation deficiencies.

4. Discussion

4.1. Spatial Resolution of Joint Inversion

The spatial resolution of the GNSS and GRACE/GFO is different, and they are suitable for respective spatial scales. Therefore, discussions on the spatial resolution of the joint inversion results are necessary. We designed two checkerboards with different spatial resolutions (2.5° × 2.5° and 3.5° × 3.5°) to test the results of the joint inversion. Figure 10a,b depicts that the white and brown checkerboards represent the EWH signals of 0 mm and 400 mm, respectively. Subsequently, we calculate the EWH from the GNSS station and the GRACE/GFO virtual station, as shown in Figure 10c,d.

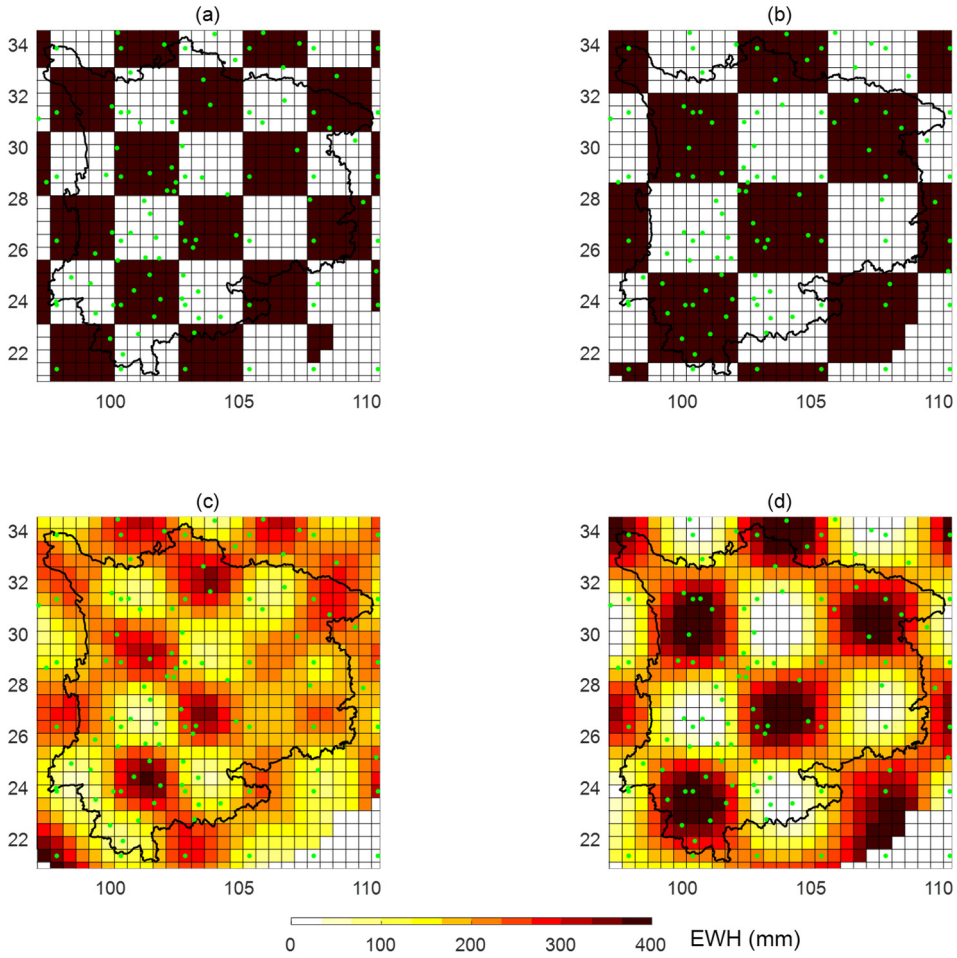


Figure 10. Joint inversion checkerboard test results. The green dots indicate the stations used for the joint inversion. (**a**) Input signals at a spatial resolution of 2.5°; (**b**) Input signal at a spatial resolution of 3.5°; (**c**) Output signal derived from joint inversion results at a spatial resolution of 2.5°; (**d**) Output signal derived from joint inversion results at a spatial resolution of 3.5°.

The joint inversion effectively recovers the EWH signal in the region. We can accurately recover the 2.5° signal in areas with densely distributed GNSS stations; however, restoring the 2.5° × 2.5° spatial resolution is less effective in regions with sparse GNSS stations and only GRACE/GFO virtual stations. For the checkerboard with a spatial resolution of 3.5° × 3.5°, only the GRACE/GFO virtual station can recover the corresponding signal (Figure S5), and the joint inversion results can also effectively recover the signal at this spatial resolution.

The checkerboard test results indicate that the joint inversion incorporating GRACE/GFO virtual stations can compensate for the spatial resolution limitation in areas with

unevenly distributed GNSS stations. This approach successfully integrates the advantages of both GNSS and GRACE/GFO satellite spatial resolutions.

4.2. Quantification of Drought Characteristics in Southwest China

The Joint-DSI is classified into five drought and wet categories based on Table S1 [56]. We have calculated the proportion of drought and flood areas to the total area of Southwest China during the study period, as shown in Figure 11. Due to distinct topographic conditions across four provinces and municipalities in Southwest China, there are different distributions of droughts and floods derived from the hydrological drought index. Following Peng et al. [38], we define drought frequency as the proportion of time when the drought index falls below D0. Therefore, this study defines drought frequency as the proportion of months with a drought index below −0.5 and then calculates the drought frequency distribution of the Joint-DSI on the monthly scale during the periods of December 2010 to June 2023 and July 2022 to June 2023, respectively (Figure 12). This scheme enables a thorough investigation of drought characteristics in Southwest China from both temporal and spatial viewpoints.

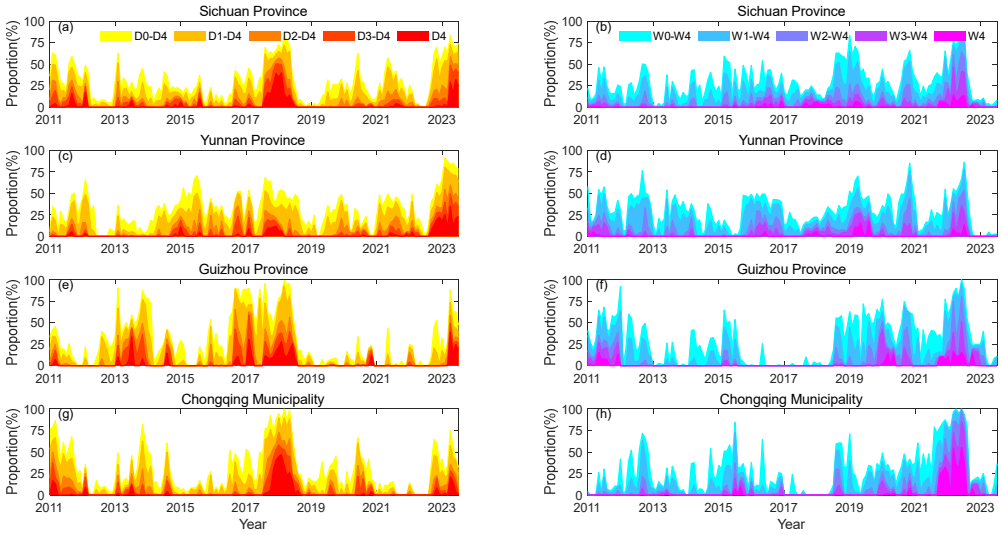


Figure 11. Drought and flood classification based on the Joint-DSI time series across four provinces and municipalities in Southwest China. (**a**) Drought classification in Sichuan Province; (**b**) Flood classification in Sichuan Province; (**c**) Drought classification in Yunnan Province; (**d**) Flood classification in Yunnan Province; (**e**) Drought classification in Guizhou Province; (**f**) Flood classification in Guizhou Province; (**g**) Drought classification in Chongqing Municipality; (**h**) Flood classification in Chongqing Municipality.

For SCP (Figure 11a,b), exceptional drought (D4) primarily occurred from July 2017 to June 2018 and October 2022 to June 2023. Approximately 39% and 32% of the SCP experienced D4 during these periods. Conversely, exceptionally wet conditions (W4) were observed mainly between September 2021 and June 2022, affecting about 14% of the area. Li et al. [33] reported that, during the 2022 drought event, drought was predominantly concentrated in the Sichuan Basin (SCB) and the western mountainous area (WTM), with SCB more severely impacted than WTM. From July 2022 to June 2023, moderate drought (D1) covered the highest proportion of the SCP, approximately 72%. The drought frequency was higher in the west and lower in the east, with the central part of the region experiencing continuous D4 (Figure 12b).

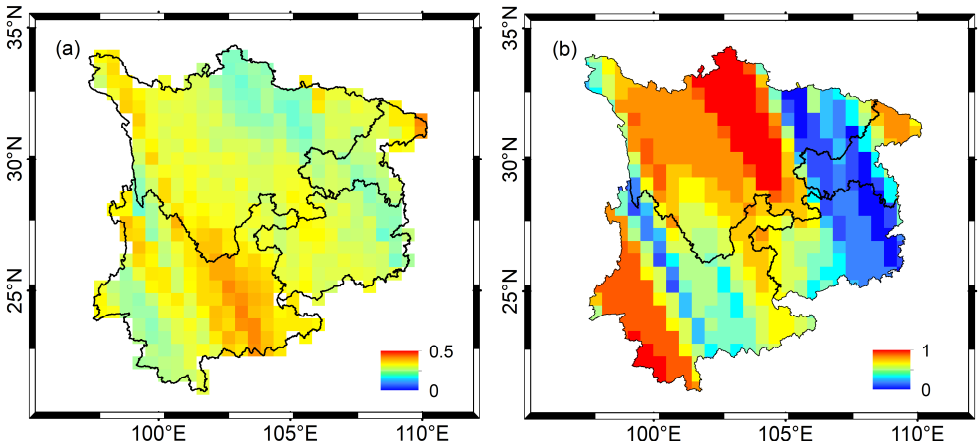


Figure 12. The Joint-DSI drought frequency distribution on a monthly scale. (**a**) represents the drought frequency distribution for 151 months from December 2010 to June 2023; (**b**) represents the drought frequency distribution for 12 months from July 2022 to June 2023.

In YNP (Figure 11c,d), D4 was most widespread from July 2017 to January 2018 and August 2022 to June 2023, impacting approximately 11% and 25% of the region in these respective periods. On the other hand, W4 conditions prevailed from January to July 2022, affecting about 13% of the area. Notably, from July 2022 to June 2023, the drought-affected area in YNP escalated to its peak, covering roughly 80% of the region. We observed that the drought frequency was lowest in the central area and highest at the peripheries, with the southwest section of the plateau experiencing persistent D4 (Figure 12b).

Regarding GZP (Figure 11e,f), D4 was primarily evident between July 2017 and June 2018, as well as from March to June 2023, affecting about 28% and 39% of GZP during these respective timeframes. On the contrary, W4 conditions were mainly noted between December 2010 and July 2011 and from October 2021 to June 2022, with approximately 15% and 16% of the region being W4, respectively. As a typical karst landscape, the intricate topography of GZP plays a significant role in its drought conditions [57]. Notably, from July 2022 to June 2023, the drought-affected area in GZP peaked, comprising roughly 73% of the total area. The drought frequency was higher in the western part and lower in the eastern part, primarily manifesting as D4 (Figure 12b).

For CQM (Figure 11g,h), D4 was particularly noticeable between July 2017 and June 2018, as well as from October 2022 to June 2023, impacting approximately 46% and 20% of CQM during these respective timeframes. Conversely, W4 conditions prevailed between October 2021 and June 2022, affecting about 55% of the region. It is worth noting that, from July 2022 to June 2023, the drought-affected area in CQM escalated to its highest proportion, roughly 57%. The drought frequency was higher in the eastern part and lower in the western part, primarily marked by D4 (Figure 12b).

The duration and intensity of D4 and wet conditions in Southwest China exhibit significant variations. We can attain a more profound comprehension of drought characteristics within this region via rigorous computations and analyses. Notably, the primary occurrences of unusual drought across various regions correspond to drought events 4 and 5, as outlined in Table 2. Specifically, drought event 4 is the most prolonged in Southwest China, whereas drought event 5 emerges as the most severe.

5. Conclusions

This paper employs multiple methods to monitor regional TWS changes, including using pure GNSS data based on Green's function and the Slepian basis function, pure GRACE/GFO Mascon data, and joint GNSS and GRACE/GFO datasets. For the inte-

grated GNSS and GRACE/GFO data, we adopt the ABIC approach to ascertain the optimal weighting factor. Additionally, we delve into drought characteristics across four provinces and municipalities in Southeast China in combination with hydrological data. The spatial distribution of TWS annual amplitudes derived from these four methods demonstrates consistency in Southwest China, with a discernible decrease from southwest to northeast. It is worth highlighting that the most pronounced annual amplitude is evident in Southwest Yunnan. In Southwestern Yunnan, GNSS-Slepian results are about 1.25 times that of GNSS-Green. Compared with GNSS results, GRACE/GFO significantly underestimated the TWS changes in Southwestern Yunnan. It is intriguing that Joint-TWS poses a stronger spatial resemblance to GRACE-TWS and demonstrates a more pronounced correlation with GRACE/GFO and dTWS/dt calculated based on the water balance equation. This enhanced correlation significantly bolsters the reliability of results in regions with sparse GNSS station coverage. Leveraging these joint inversion results, we have successfully tracked five drought events in Southwest China from December 2010 to June 2023. Among these events, the fifth is the most severe regarding the water deficit. We perform individual computations and analyses for SCP, YNP, CQM, and GZP to investigate drought characteristics better. The results reveal that all regions exhibit remarkable drought characteristics during the fifth drought event, accompanied by widespread drought indicators. Our research indicates that integrating GNSS and GRACE/GFO data for TWS change inversion can effectively compensate for the constraints posed by uneven GNSS station distribution, as well as the inherent challenges of limited resolution and incompleteness of GRACE/GFO data, and provide an alternative for monitoring regional TWS changes and drought conditions using geodetic data.

Supplementary Materials: The following supporting information can be downloaded at: https://www.mdpi.com/article/10.3390/rs17030397/s1, Figure S1: (a) Annual amplitude of GNSS vertical displacement under non-tidal atmospheric loading effects; (b) annual amplitude of GNSS vertical surface displacement under non-tidal ocean loading effects; (c) annual amplitude of GNSS vertical crustal displacement after post-processing; Figure S2: Determination of regularization factor from Green's function inversion by GCV method; Figure S3: Concentration ratio of each Slepian basis function. Figure S4: Energy spatial distribution of Slepian basis functions, with the black solid line indicating the boundary of the study region after an extension of 2°. Figure S5: Checkerboard test results from GRACE/GFO virtual station. Figure S6: Spatial evolution of hydrological drought in Southwest China from July 2022 to June 2023, with the legend representing the Joint-DSI values. Table S1: Classification of drought severity.

Author Contributions: Funding acquisition, L.L. and T.W.; Conceptualization, N.C.; Data curation, Z.L.; Investigation, L.L. and X.L.; Methodology, X.L. and N.C.; Validation, T.W. and X.L.; Writing—original draft, L.L., X.L. and T.W.; Writing—review & editing, N.C., and Z.L. All authors have read and agreed to the published version of the manuscript.

Funding: This research is funded by the National Natural Science Foundation of China (42264003, 42274115 and 41974019), Ganpo Juncai Support Program for Academic and Technical Leaders of Major Disciplines Training Project (20232BCJ23018), Jiangxi Province Natural Science Foundation (20224BAB213048), and Doctoral Research Startup Fund of East China University of Technology (DHBK2019182).

Data Availability Statement: GNSS time series are available from CMONOC (http://www.eqdsc.com, accessed on 1 May 2024). NTOL and NTAL models are provided by GFZ (http://esmdata.gfz-potsdam.de:8080/repository, accessed on 30 May 2024). The GRACE RL06 Mascon Grids are released by CSR (https://www2.csr.utexas.edu/grace/RL06_mascons.html, accessed on 1 June 2024). The ERA5-Land datasets are derived from ECMWF (https://cds.climate.copernicus.eu/, accessed on 30 June 2024). The GLDAS data originates from Goddard Earth Sciences Data and Information Services (https://disc.gsfc.nasa.gov/, accessed on 30 June 2024). The GPCP precipitation data comes

from the National Centers for Environmental Information. (https://www.ncei.noaa.gov/, accessed on 30 June 2024). The GLEAM evapotranspiration data derived from https://www.gleam.eu/, accessed on 30 June 2024. The SPEI is provided by the Climate Research Center (CRU) at the University of East Anglia (https://digital.csic.es/, accessed on 30 June 2024).

Acknowledgments: The authors would like to acknowledge the CMONOC for providing GNSS vertical displacement data; thank the CSR for GRACE/GFO Mascon; thank the ERA5, NOAH, and GPCP for the monthly precipitation data; thank GLEAM, ERA5, and NOAH for the monthly evaporation data; thank ERA5 and NOAH for the monthly runoff data; and thank CRU for SPEI data.

Conflicts of Interest: The authors declare no conflicts of interest.

References

1. Huang, J.; Li, Y.; Fu, C.; Chen, F.; Fu, Q.; Dai, A.; Shinoda, M.; Ma, Z.; Guo, W.; Li, Z.; et al. Dryland climate change: Recent progress and challenges. *Rev. Geophys.* **2017**, *55*, 719–778. [CrossRef]
2. Han, L.; Zhang, Q.; Zhang, Z.; Jia, J.; Wang, Y.; Huang, T.; Cheng, Y. Drought area, intensity and frequency changes in China under climate warming, 1961–2014. *J. Arid Environ.* **2021**, *193*, 104596. [CrossRef]
3. Yuan, X.; Wang, Y.; Ji, P.; Wu, P.; Sheffield, J.; Otkin, J.A. A global transition to flash droughts under climate change. *Science* **2023**, *380*, 187–191. [CrossRef]
4. Zhou, L.; Yang, G. Ecological Economic Problems and Development Patterns of the Arid Inland River Basin in Northwest China. *Ambio* **2006**, *35*, 316–318. [CrossRef]
5. Mishra, A.K.; Singh, V.P. A review of drought concepts. *J. Hydrol.* **2010**, *391*, 202–216. [CrossRef]
6. Qiu, K.; You, W.; Jiang, Z.; Tang, M. Tracking the water storage and runoff variations in the Parana' basin via GNSS measurements. *Sci. Total Environ.* **2023**, *912*, 168831. [CrossRef] [PubMed]
7. Boeing, F.; Wagener, T.; Marx, A.; Rakovec, O.; Kumar, R.; Samaniego, L.; Attinger, S. Increasing influence of evapotranspiration on prolonged water storage recovery in Germany. *Environ. Res. Lett.* **2024**, *19*, 024047. [CrossRef]
8. Zhu, H.; Chen, K.; Hu, S.; Wang, J.; Wang, Z.; Li, J.; Liu, J. A novel GNSS and precipitation-based integrated drought characterization framework incorporating both meteorological and hydrological indicators. *Remote Sens. Environ.* **2024**, *311*, 114261. [CrossRef]
9. Rodell, M.; Famiglietti, J.S. Detectability of variations in continental water storage from satellite observations of the time dependent gravity field. *Water Resour. Res.* **1999**, *35*, 2705–2723. [CrossRef]
10. Tapley, B.D.; Bettadpur, S.; Ries, J.C.; Thompson, P.F.; Watkins, M.M. GRACE measurements of mass variability in the Earth system. *Science* **2004**, *305*, 503–505. [CrossRef]
11. Swenson, S.; Wahr, J. Post-processing removal of correlated errors in GRACE data. *Geophys. Res. Lett.* **2006**, *33*, L08402. [CrossRef]
12. Scanlon, B.R.; Zhang, Z.; Save, H.; Bierkens, M.F.P. Global models underestimate large decadal declining and rising waterstorage trends relative to GRACE satellite data. *Proc. Natl. Acad. Sci. USA* **2018**, *115*, E1080–E1089. [CrossRef] [PubMed]
13. Farrell, W.E. Deformation of the Earth by surface loads. *Rev. Geophys.* **1972**, *10*, 761–797. [CrossRef]
14. Wu, X.P.; Heflin, M.B.; Ivins, E.R.; Argus, D.F.; Webb, F.H. Large-scale global surface mass variations inferred from GPS measurements of load-induced deformation. *Geophys. Res. Lett.* **2003**, *30*, 1742. [CrossRef]
15. Wahr, J.; Khan, S.A.; Dam, T.V.; Liu, L.; Angelen, J.H.V.; Broeke, M.R.V.D.; Meertens, C.M. The use of GPS horizontals for loading studies, with applications to northern California and southeast Greenland. *J. Geophys. Res. Solid Earth* **2013**, *118*, 1795–1806. [CrossRef]
16. White, A.M.; Gardner, W.P.; Borsa, A.A.; Argus, D.F.; Martens, H.R. A review of GNSS/GPS in hydrogeodesy: Hydrologic loading applications and their implications for water resource research. *Water Resour. Res.* **2022**, *58*, e2022WR032078. [CrossRef] [PubMed]
17. Li, J.C.; Li, X.P.; Zhong, B. Review of Inverting GNSS Surface Deformations for Regional Terrestrial Water Storage Changes. *Geomat. Inf. Sci. Wuhan Univ.* **2023**, *48*, 1724–1735.
18. Han, S.-C.; Razeghi, S.M. GPS Recovery of Daily Hydrologic and Atmospheric Mass Variation: A Methodology and Results from the Australian Continent. *J. Geophys. Res. Solid Earth* **2017**, *122*, 9328–9343. [CrossRef]
19. Argus, D.F.; Fu, Y.N.; Landerer, F.W. Seasonal variation in total water storage in California inferred from GPS observations of vertical land motion. *Geophys. Res. Lett.* **2014**, *41*, 1971–1980. [CrossRef]
20. Fu, Y.N.; Argus, D.F.; Landerer, F.W. GPS as an independent measurement to estimate terrestrial water storage variations in Washington and Oregon. *J. Geophys. Res. Solid Earth* **2015**, *120*, 552–566. [CrossRef]
21. Jiang, Z.S.; Hsu, Y.J.; Yuan, L.G.; Yang, X.C.; Ding, Y.H.; Tang, M.; Chen, C.F. Characterizing spatiotemporal patterns of terrestrial water storage variations using GNSS vertical data in Sichuan, China. *J. Geophys. Res. Solid Earth* **2021**, *126*, e2021JB022398. [CrossRef]

22. Li, X.P.; Zhong, B.; Li, J.C.; Liu, R.L. Inversion of GNSS Vertical Displacements for Terrestrial Water Storage Changes Using Slepian Basis Functions. *Earth Space Sci.* **2023**, *10*, e2022EA002608. [CrossRef]
23. Pintori, F.; Serpelloni, E. Drought-Induced Vertical Displacements and Water Loss in the Po River Basin (Northern Italy) From GNSS Measurements. *Earth Space Sci.* **2024**, *11*, e2023EA003326. [CrossRef]
24. Wang, S.-Y.; Li, J.; Chen, J.; Hu, X.-G. On the Improvement of Mass Load Inversion with GNSS Horizontal Deformation: A Synthetic Study in Central China. *J. Geophys. Res. Solid Earth* **2022**, *127*, e2021JB023696. [CrossRef]
25. Fok, H.S.; Liu, Y. An improved GPS-inferred seasonal terrestrial water storage using terrain-corrected vertical crustal displacements constrained by GRACE. *Remote Sens.* **2019**, *11*, 1433. [CrossRef]
26. Liu, Y.; Fok, H.S.; Tenzer, R.; Chen, Q.; Chen, X. Akaike's Bayesian Information Criterion for the Joint Inversion of Terrestrial Water Storage Using GPS Vertical Displacements, GRACE and GLDAS in Southwest China. *Entropy* **2019**, *21*, 664. [CrossRef] [PubMed]
27. Li, X.P.; Zhong, B.; Li, J.C.; Liu, R.L. Joint inversion of GNSS and GRACE/GFO data for terrestrial water storage changes in the Yangtze River Basin. *Geophys. J. Int.* **2023**, *233*, 1596–1616. [CrossRef]
28. Zhu, H.; Chen, K.; Hu, S.; Wei, G.; Chai, H.; Wang, T. Characterizing hydrological droughts within three watersheds in Yunnan, China from GNSS-inferred terrestrial water storage changes constrained by GRACE data. *Geophys. J. Int.* **2023**, *235*, 1581–1599. [CrossRef]
29. Adusumilli, S.; Borsa, A.A.; Fish, M.A.; McMillan, H.K.; Silverii, F. A Decade of Water Storage Changes Across the Contiguous United States from GPS and satellite gravity. *Geophys. Res. Lett.* **2019**, *46*, 13006–13015. [CrossRef]
30. Carlson, G.; Werth, S.; Shirzaei, M. Joint Inversion of GNSS and GRACE for Terrestrial Water Storage Change in California. *J. Geophys. Res. Solid Earth* **2022**, *127*, e2021JB023135. [CrossRef] [PubMed]
31. Yang, X.; Yuan, L.; Jiang, Z.; Tang, M.; Feng, X.; Li, C. Investigating terrestrial water storage changes in Southwest China by integrating GNSS and GRACE/GRACE-FO observations. *J. Hydrol. Reg. Stud.* **2023**, *48*, 101457. [CrossRef]
32. Ge, Y.K.; Zhao, L.L.; Chen, J.S.; Ren, Y.N.; Li, H.Z. Spatio-temporal Evolution Trend of Meteorological Drought and Identification of Drought Events in Southwest China from 1983 to 2020. *Ecol. Environ. Sci.* **2023**, *32*, 920–932.
33. Shi, P.; Tang, H.; Qu, S.M.; Wen, T.; Zhao, L.L.; LI, Q.F. Characteristics of propagation from meteorological drought to hydrological drought in Southwest China. *Water Resour. Prot.* **2023**, *39*, 49–56.
34. Jiang, Z.S.; Hsu, Y.-J.; Yuan, L.G.; Huang, D.F. Monitoring time-varying terrestrial water storage changes using daily GNSS measurements in Yunnan, southwest China. *Remote Sens. Environ.* **2021**, *254*, 112249. [CrossRef]
35. Li, X.P.; Zhong, B.; Chen, J.L.; Cheng Li, J.; Wang, H.H. Investigation of 2020–2022 extreme floods and droughts in Sichuan Province of China based on joint inversion of GNSS and GRACE/GFO data. *J. Hydrol.* **2024**, *2024*, 130868. [CrossRef]
36. Chen, H.; Sun, J. Changes in Drought Characteristics over China Using the Standardized Precipitation Evapotranspiration Index. *J. Clim.* **2015**, *28*, 5430–5447. [CrossRef]
37. Yao, C.L.; Luo, Z.C.; Wang, C.; Zhang, R.; Li, J.M. Detecting droughts in Southwest China from GPS vertical position displacements. *Acta Geod. Cartogr. Sin.* **2019**, *48*, 547–554.
38. Peng, Y.J.; Chen, G.; Chao, N.F.; Wang, Z.T.; Wu, T.T.; Luo, X.Y. Detection of extreme hydrological droughts in the poyang lake basin during 2021–2022 using GNSS-derived daily terrestrial water storage anomalies. *Sci. Total Environ.* **2024**, *919*, 170875. [CrossRef] [PubMed]
39. Zhu, H.; Chen, K.; Chai, H.; Ye, Y.; Liu, W. Characterizing extreme drought and wetness in Guangdong, China using global navigation satellite system and precipitation data. *Satell. Navig.* **2024**, *5*, 1. [CrossRef]
40. Herring, T.A.; King, R.W.; Floyd, M.A.; McClusky, S.C. *Introduction to GAMIT/GLOBK, Release 10.7*; Massachusetts Institute of Technology: Cambridge, MA, USA, 2018.
41. Dong, D.; Herring, T.; King, R.W. Estimating regional deformation from a combination of space and terrestrial geodetic data. *J. Geod.* **1998**, *72*, 200–214. [CrossRef]
42. Liu, N.; Dai, W.J.; Santerre, R.; Kuang, C.L. A MATLAB-based Kriged Kalman Filter software for interpolating missing data in GNSS coordinate time series. *GPS Solut.* **2018**, *22*, 25. [CrossRef]
43. Save, H.; Bettadpur, S.; Tapley, B.D. High-resolution CSR GRACE RL05 mascons. *J. Geophys. Res. Solid Earth* **2016**, *121*, 7547–7569. [CrossRef]
44. Zhang, L.; Sun, W.K. Progress and prospect of GRACE Mascon product and its application. *Rev. Geophys. Planet. Physics* **2022**, *53*, 35–52.
45. Muñoz Sabater, J. ERA5-Land Hourly Data from 1950 to Present. Opernicus Climate Change Service (C3S) Climate Data Store (CDS). 2019. Available online: https://cds.climate.copernicus.eu/datasets/reanalysis-era5-land-monthly-means?tab=overview (accessed on 30 June 2024).
46. Rodell, M.; Houser, P.; Jambor, U.; Gottschalck, J.; Mitchell, K.; Meng, C.-J.; Arsenault, K.; Cosgrove, B.; Radakovich, J.; Bosilovich, M. The global land data assimilation system. *Bull. Am. Meteorol. Soc.* **2004**, *85*, 381–394. [CrossRef]

47. Adler, R.F.; Huffman, G.J.; Chang, A.; Ferraro, R.; Xie, P.-P.; Janowiak, J.; Rudolf, B.; Schneider, U.; Curtis, S.; Bolvin, D.; et al. The Version-2 Global Precipitation Climatology Project (GPCP) Monthly Precipitation Analysis (1979–Present). *J. Hydrometeorol.* **2003**, *4*, 1147–1167. [CrossRef]
48. Miralles, D.G.; Holmes, T.R.H.; Jeu, R.A.M.D.; Gash, J.H.; Meesters, A.G.C.A.; Dolman, A.J. Global land-surface evaporation estimated from satellite-based observations. *Hydrol. Earth Syst. Sci.* **2011**, *15*, 453–469. [CrossRef]
49. Chen, J.; Tapley, B.; Rodell, M.; Seo, K.W.; Wilson, C.; Scanlon, B.R.; Pokhrel, Y. Basin-Scale River Runoff Estimation from GRACE Gravity Satellites, Climate Models, and In Situ Observations: A Case Study in the Amazon Basin. *Water Resour. Res.* **2020**, *56*, e2020WR028032. [CrossRef]
50. Landerer, F.W.; Dickey, J.O.; Güntner, A. Terrestrial water budget of the Eurasian pan-Arctic from GRACE satellite measurements during 2003–2009. *J. Geophys. Res. Atmos.* **2010**, *115*, D23. [CrossRef]
51. Funning, G.J.; Fukahata, Y.; Yagi, Y.; Parsons, B. A method for the joint inversion of geodetic and seismic waveform data using ABIC: Application to the 1997 Manyi, Tibet, earthquake. *Geophys. J. Int.* **2014**, *196*, 1564–1579. [CrossRef]
52. Fukahata, Y.; Nishitani, A.; Matsu'ura, M. Geodetic data inversion using ABIC to estimate slip history during one earthquake cycle with viscoelastic slip-response functions. *Geophys. J. Int.* **2010**, *156*, 140–153. [CrossRef]
53. Thomas, A.C.; Reager, J.T.; Famiglietti, J.S.; Rodell, M. A GRACE- based water storage deficit approach for hydrological drought characterization. *Geophys. Res. Lett.* **2014**, *41*, 1537–1545. [CrossRef]
54. Chen, C.; Zou, R.; Fang, Z.; Cao, J.; Wang, Q. Using geodetic measurements derived terrestrial water storage to investigate the characteristics of drought in Yunnan, China. *GPS Solut.* **2023**, *28*, 51. [CrossRef]
55. Hsu, Y.-J.; Fu, Y.; Bürgmann, R.; Hsu, S.-Y.; Lin, C.-C.; Tang, C.-H.; Wu, Y.-M. Assessing seasonal and interannual water storage variations in Taiwan using geodetic and hydrological data. *Earth Planet. Sci. Lett.* **2020**, *550*, 116532. [CrossRef]
56. Zhao, M.; Aa, G.; Velicogna, I.; Kimball, J.S. Satellite Observations of Regional Drought Severity in the Continental United States Using GRACE-Based Terrestrial Water Storage Changes. *J. Clim.* **2017**, *30*, 6297–6308. [CrossRef]
57. Mao, C.Y.; Dai, L.; Yang, G.B.; Yin, C.Y.; Yang, Q.; Liu, F.; Li, M. Dynamic analysis of spatio-temporal distribution of droughts in karst mountainous regions of Guizhou Province from 1960 to 2016. *J. Water Resour. Water Eng.* **2021**, *32*, 64–72+79.

Disclaimer/Publisher's Note: The statements, opinions and data contained in all publications are solely those of the individual author(s) and contributor(s) and not of MDPI and/or the editor(s). MDPI and/or the editor(s) disclaim responsibility for any injury to people or property resulting from any ideas, methods, instructions or products referred to in the content.